Topology-dependent levitation-force degradation induced by angular interfacial gaps in segmented YBCO bulks

Yuan Liu(刘源), Xiping Ding(丁西平), Yulong Guo(郭玉龙), Xianfeng Zhao*(赵宪锋)

School of Civil Engineering, Lanzhou Jiaotong University, Lanzhou 730070, Gansu, China.

*E-mail: zhaoxf@mail.lzjtu.cn

Abstract

High-temperature superconducting levitation is a promising technology for future high-speed transportation. This numerical study investigates levitation-force degradation caused by an angular interfacial gap in a segmented two-YBCO-bulk configuration and its dependence on the spatial matching between permanent-magnet-guideway (PMG) field topology and gap location. Among the three guideways considered, the flux-concentrating PMG shows the largest reduction in peak levitation force (24.58% at $\theta = 5°$), whereas the Halbach PMG shows the smallest reduction (7.12%). Formation of a finite gap changes the contacting interface into two exposed electromagnetic boundaries, reconstructs the shielding-current paths, generates an unfavorable local Lorentz-force contribution near the gap, and weakens the dominant positive-force region. The large initial reduction for the flux-concentrating and surface-magnetized PMGs is therefore attributed primarily to loss of electromagnetic continuity when the finite gap first forms; subsequent increases in angle have a weaker secondary effect. The results provide quantitative guidance for the segmented HTS configurations investigated here. Direct quantitative extrapolation to microscopic defects is not intended because their length scales, aspect ratios, material properties, and local boundary conditions may differ.

Keywords

high-temperature superconductor; permanent magnet guideway; levitation force; geometric discontinuity

PACS

85.70.Rp, 74.25.Ha, 74.25.Sv, 74.25.Wx

1. Introduction

High-temperature superconducting (HTS) magnetic levitation has attracted sustained attention because of its passive stability, non-contact operation, low mechanical loss, and high load capacity. These characteristics make HTS levitation systems promising for high-speed transportation, superconducting bearings, flywheel energy storage, and precision positioning [1–6]. In a typical system, bulk superconductors interact with the magnetic field generated by a permanent magnet guideway (PMG). The induced shielding currents and flux pinning provide stable levitation without active feedback control and constitute the physical basis of HTS pinning maglev systems.

HTS maglev research has progressed from laboratory-scale demonstrations to engineering test platforms, vehicle prototypes, and system-level performance evaluation. At this stage, levitation force, guidance stiffness, structural reliability, and environmental adaptability must be considered together. Representative milestones include the first manned HTS maglev test vehicle [7], a 45 m ring test line in Chengdu for vehicle-dynamics and guideway studies [8],

and systematic assessments of engineering challenges and aerodynamic safety [9,10]. These developments show that HTS maglev research has entered a stage in which coupled system-level effects require explicit consideration.

PMG design is a critical aspect of system-level HTS maglev research because the spatial distribution of the guideway field governs flux penetration, shielding-current evolution, and electromagnetic-force generation. Previous optimization studies have addressed field enhancement, force improvement, guidance stability, and material utilization. Examples include Halbach PMGs designed to enhance the working-side magnetic field and the levitation and guidance forces [11], single-peak and V-shaped combined PMGs [12], guideways designed for curve negotiation [13], and double-layer quasi-Halbach guideways that reduce rare-earth-magnet consumption while maintaining magnetic performance [14]. These studies demonstrate that PMG topology is an important factor controlling flux penetration and shielding-current distribution.

Levitation performance is governed not only by the guideway field but also by the structural and assembly integrity of the HTS bulks. At the assembly scale, the limited dimensions of single-grain bulks and the demand for larger levitation surfaces often require several bulks to be arranged together. Manufacturing tolerances, assembly errors, local support deformation, or slight relative rotation between adjacent bulks can produce a nonuniform wedge-shaped interfacial opening. An angular gap therefore provides a simplified representation of rotational misalignment between adjacent bulks, unlike a parallel translational gap with constant separation. At the material scale, cracks, inclusions, pores, and grain-boundary gaps may arise from the brittleness of ceramic superconductors [4,12] and from electromagnetic stresses and thermal gradients during cooling, magnetization, and service [15,16]. Pulsed-field magnetization can also initiate cracks in bulk superconductors [17]. Although assembly gaps and material defects differ substantially in scale and constitution, both can perturb local shielding-current paths and magnetic-flux penetration [18,19].

Previous studies have examined several electromagnetic and mechanical consequences of discontinuities. Houbart et al [20] investigated electromagnetic coupling between adjacent magnetized bulks, and Tutt et al [21] examined the effects of joint interfaces between GdBCO bulks on current transfer and trapped-field performance. Shi et al [16] showed that microstructural features can influence the critical-current-density distribution and trapped-field uniformity of REBCO single grains. Other studies considered crack propagation under field magnetization [22], crack effects on nonlinear vibration of maglev systems [23], multiple edge cracks in REBCO tapes [24], dynamic fracture during pulsed-field magnetization [25], and current redistribution around elliptical flaws in bulk superconductors [26]. Most of these studies focus on a particular discontinuity or loading condition; systematic comparisons of how a prescribed interfacial orientation interacts with different PMG field topologies remain limited.

The present study therefore examines the combined effects of field topology and an angular interfacial gap. The three PMG configurations generate distinct field profiles, whereas rotation of the two adjacent bulks changes the location and orientation of the exposed gap boundaries relative to those profiles. The working hypothesis is that the response of a segmented HTS assembly is governed by spatial matching between the local field distribution and the interfacial gap. The study is confined to a macroscopic air gap between two adjacent bulks. It does not assume quantitative equivalence with microscopic cracks or inclusions, whose characteristic dimensions, aspect ratios, material properties, and local electromagnetic boundary conditions may be substantially different.

The H-formulation has been widely used to describe nonlinear E–J behavior, flux penetration, and time-dependent current redistribution in HTS materials [27–34]. Its applications have mainly addressed continuous superconductors or specified defect geometries. Although a macroscopic H-formulation model cannot resolve individual vortices or microscopic pinning processes, it can describe engineering-scale current rerouting and force-density redistribution around electrically blocking boundaries. Cross-scale studies of vortex pinning [35] further indicate the importance of connecting fundamental superconducting physics with engineering-scale response. Accordingly, the present results are interpreted as a macroscopic analysis of segmented HTS assemblies; any analogy with microscopic defects is qualitative and requires separate scale-resolved validation.

A two-dimensional H-formulation model is used to investigate a prescribed angular air gap between two adjacent YBCO bulks while keeping the total superconducting cross-sectional area constant. The levitation-force response is compared under flux-concentrating, surface-magnetized, and Halbach PMGs. Magnetic-field distributions, shielding-current density, the internal horizontal magnetic-flux-density component, and Lorentz body-force density are analyzed to determine how PMG field topology controls the current reconstruction caused by formation and enlargement of the gap.

2. Numerical modelling and simulation setup

2.1 H-formulation methodology

In numerical simulations of HTS, the H-formulation takes the magnetic field intensity $\boldsymbol{H}$ as the sole primary unknown and unifies the Maxwell-Faraday equation, Ampère's law, and the constitutive relations into a single vector PDE in $\boldsymbol{H}$, which serves as the governing equation for the HTS maglev system. The Maxwell Faraday model is expressed as follows:

$$\nabla \times \boldsymbol{E} = -\frac{\partial \boldsymbol{B}}{\partial t} \tag{1}$$

$$\nabla \times \boldsymbol{H} = \boldsymbol{J} \tag{2}$$

$$\boldsymbol{B} = \mu_0 \mu_r \boldsymbol{H} \tag{3}$$

$$\boldsymbol{E} = \rho \boldsymbol{J} \tag{4}$$

where $\boldsymbol{E}$ is the electric field strength, $\boldsymbol{B}$ is the magnetic flux density, $\boldsymbol{H}$ is the magnetic field intensity, $\boldsymbol{J}$ is the current density, μ_0 is the vacuum permeability, μ_r is the relative permeability and ρ is the electrical resistivity.

The HTS is described by the power-law E–J relation and the empirical isotropic Kim-like model [36]:

$$\boldsymbol{E} = E_0 \left(\frac{|\boldsymbol{J}|}{J_c(B)}\right)^{n-1} \boldsymbol{J} \tag{5}$$

$$J_c = \frac{J_{c0}}{1 + |\boldsymbol{B}/B_0|} \tag{6}$$

where J_c is the critical current density, B_0 is the characteristic magnetic field, E_0 is the reference electric field, and n is the power-law exponent. Substituting the $\boldsymbol{E}$-$\boldsymbol{J}$ constitutive relation (Eqs. (5) and (6)) into Maxwell's equations (Eqs. (1)-(4)) yields the governing equation in terms of $\boldsymbol{H}$:

$$\mu_0 \mu_r \frac{\partial \boldsymbol{H}}{\partial t} + \nabla \times [\rho(|\nabla \times \boldsymbol{H}|) \nabla \times \boldsymbol{H}] = 0 \tag{7}$$

When the HTS moves relative to the magnetic field of the PMs, the interaction between the shielding currents and the magnetic field produces a force. The total force $\boldsymbol{F}$ is given by the volume integral of the Lorentz force density:

$$\boldsymbol{F} = \int_{\Omega_{SC}} \boldsymbol{J} \times \boldsymbol{B} dV \tag{8}$$

where Ω_{sc} is the superconducting domain and V denotes the volume occupied by the shielding currents.

2.2 HTS–PMG model

Three PMG configurations are considered: a flux-concentrating PMG (FCPMG), a surface-magnetized PMG (SMPMG), and a Halbach PMG (HPMG). The model contains two adjacent YBCO regions, as shown in figures 1(a)–1(c). For the reference case θ = 0°, the regions are joined and treated as a single electromagnetically continuous superconducting domain; no internal boundary condition is imposed to block current transfer across their common interface. For every θ > 0°, rotation creates an air gap and the two YBCO regions become spatially and electromagnetically separated. Current cannot cross the air gap, and the two newly exposed inner surfaces act as superconducting–air boundaries. Consequently, the comparison between θ = 0° and the smallest nonzero angle measures primarily the effect of changing from a continuous joined domain to two separated superconducting domains. Comparisons among the nonzero-angle cases quantify the additional effect of increasing the angular opening after separation has occurred.

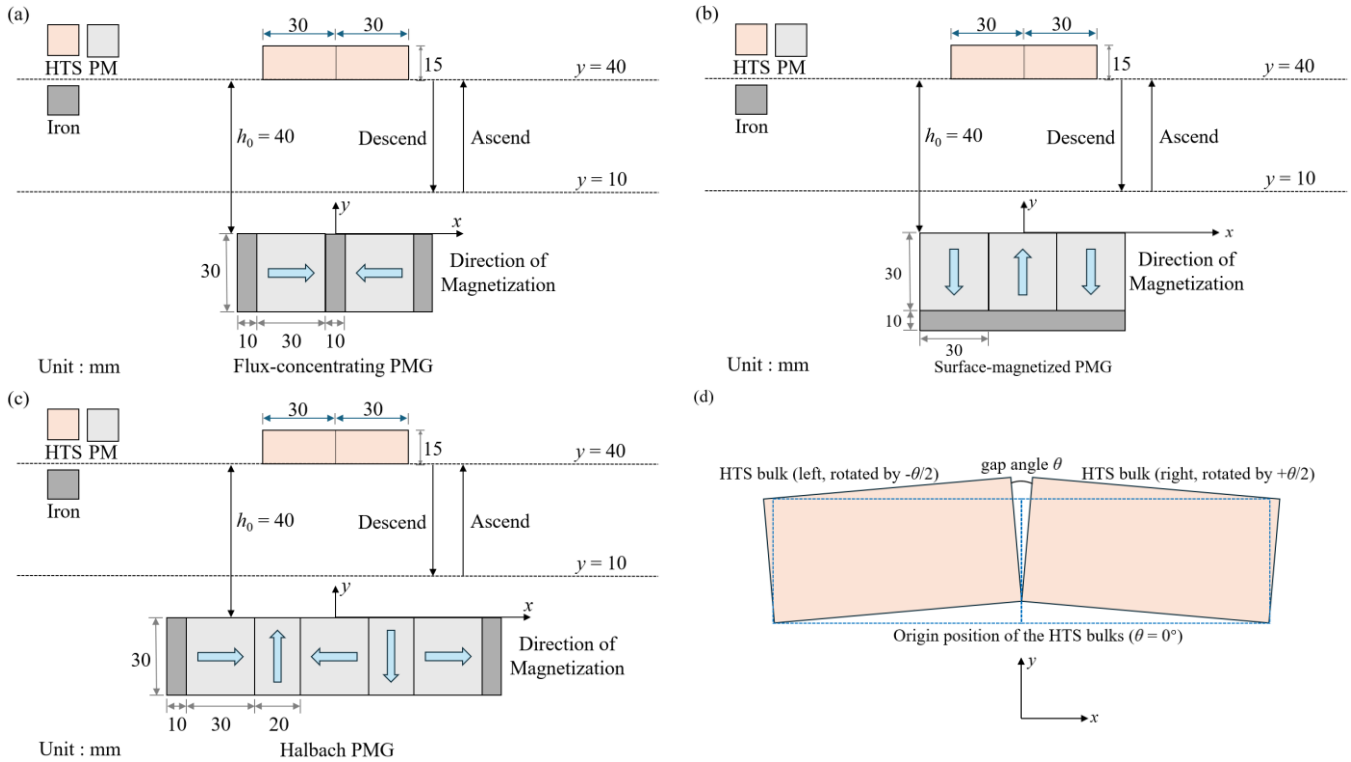


Figure 1. Schematic of the two-dimensional HTS–PMG system and its vertical motion process. (a) Flux-concentrating PMG; (b) Surface-magnetized PMG; (c) Halbach PMG; (d) definition of the inclination angle θ of the HTS bulks.

To ensure a consistent comparison with the conventional single bulk case, the total cross sectional area of the two superconducting bulks is kept identical to that of the original bulk.

The PMG is composed of NdFeB permanent magnets with a residual magnetic flux density of $B_r = 0.4$ T. The geometric dimensions and material parameters of the superconducting bulks and the PMG are summarized in figure 1. As shown in figure 1(d), the angular gap is introduced by symmetrically rotating the two superconducting bulks about their common centerline. This configuration represents relative angular misalignment between adjacent bulks in a segmented HTS assembly. It is defined as the

wedge-shaped space between the bulks, and its magnitude is quantified by the angle θ, which ranges from 0° to 5° in this study. Different gap angles are considered to evaluate their influence on the electromagnetic behavior and levitation performance. The electromagnetic properties of the HTS bulk are described using the power-law E–J constitutive relation combined with the Kim critical current model. The key parameters are $J_{c0} = 1.1 \times 10^8$ Am^{-2}, $B_0 = 0.38$ T, $E_0 = 1.0 \times 10^{-4}$ Vm^{-1}, and $n = 21$.

The values of J_{c0} and n are selected according to representative electromagnetic properties of melt-processed YBCO bulks reported in the literature. The characteristic magnetic field B_0 is calibrated by comparison with existing levitation force measurements to ensure a reasonable representation of the superconducting electromagnetic response.

A quasi-static numerical procedure is adopted. After zero-field cooling at a levitation height of 40 mm, the bulks move vertically from 40 to 10 mm and then return to 40 mm, completing a loading–unloading cycle. The prescribed velocity is 1 mm s^{-1}, so each 30 mm branch lasts 30 s and the applied field changes slowly along the motion path. This velocity and moving-domain treatment are consistent with the framework previously compared with measurements in Ref. [37]. The calculated magnetic-flux-density, shielding-current-density, and levitation-force histories are recorded throughout the cycle. The term quasi-static here refers to the prescribed slow mechanical motion; the time-dependent electromagnetic response and hysteresis remain explicitly represented by the H-formulation and power-law E–J relation.

The numerical framework adopted here is based on that used in Ref. [37], in which the calculated magnetic-field components above a Halbach PM track and the levitation-force–height response were compared with the experimental data reported in Ref. [33]. The model reproduced the measured field amplitude and spatial periodicity, as well as the overall trend and magnitude of the levitation-force curve. A local discrepancy was observed near x = ±40 mm, where the two-dimensional model slightly overestimated the magnetic-field peaks. This discrepancy was attributed mainly to the neglect of longitudinal end effects and three-dimensional current closure, together with geometric simplification, material-parameter uncertainty, and numerical discretization. Ref. [37] did not report consolidated error metrics such as the maximum error, RMSE, or R^2. Therefore, the comparison provides qualitative and graphical validation of the H-formulation, material-parameter set, and low-speed moving-process treatment, but it does not constitute direct experimental validation of all three PMG configurations or of the angular-gap geometry investigated in the present study.

3. Electromagnetic field and shielding current redistribution characteristics

3.1 Magnetic field distribution

Before discussing the shielding current redistribution and levitation force response of two-YBCO-bulk configuration, the magnetic field characteristics of the three PMG configurations are first examined. Since the external magnetic field generated by the guideway serves as the excitation source for flux penetration in the superconductors, its amplitude, spatial distribution, and gradient directly determine the subsequent current activation, current path reconstruction, and electromagnetic force generation. Therefore, the magnetic flux density magnitude |B| distributions above the flux-concentrating PMG (FCPMG), surface-magnetized PMG (SMPMG), and Halbach PMG (HPMG) are compared at different levitation heights, as shown in figure 2.

The magnetic flux density increases as the levitation height decreases for all three guideways, but its spatial distribution depends strongly on PMG topology. The FCPMG has a sharp central peak produced by flux concentration through the iron poles [11]. The SMPMG produces a smoother and weaker central field, with smaller lateral gradients [13]. The HPMG generates the highest overall field and a double-peak distribution arising from superposition of fields produced by magnets with different magnetization directions [38,39]. Halbach arrangements can also improve utilization of permanent magnet material [14].

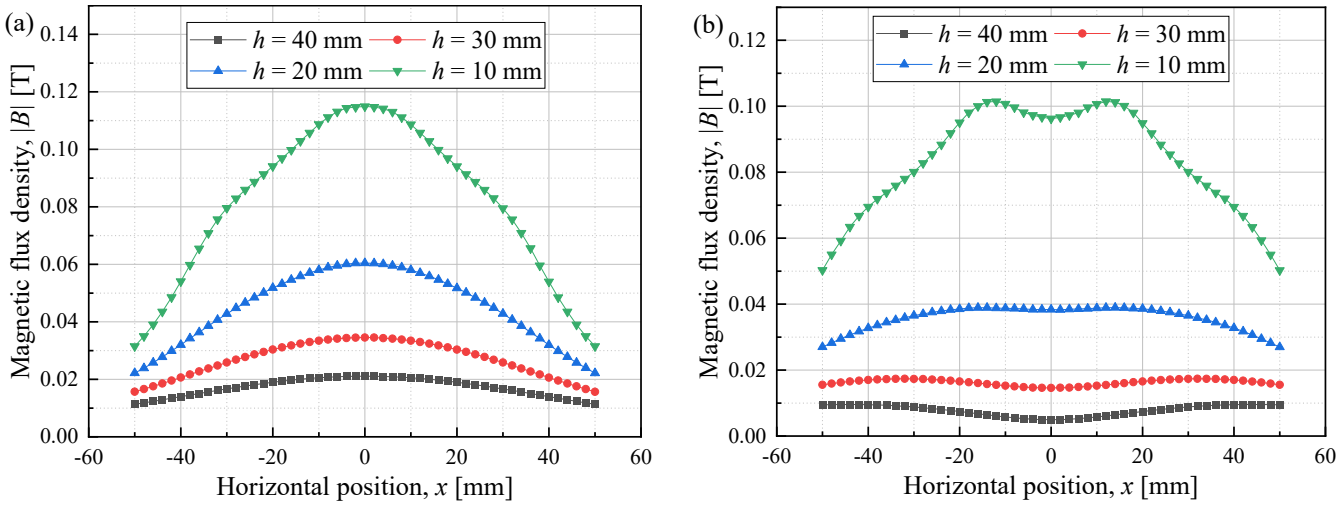
The distinct magnetic field characteristics of the three PMG configurations at the centreline (10 mm above the guideway) can be summarised as follows. At this height, the FCPMG produces a peak field of approximately 0.115 T at the centre, with the field dropping to half of its peak value within ±39 mm laterally, resulting in the largest horizontal field gradient among the three configurations. The SMPMG generates a more uniform field with a peak value of about 0.101 T and the smallest spatial gradient, showing less than 10% variation over a ±24 mm range. The HPMG, by contrast, exhibits a double-peak profile with two symmetric maxima of approximately 0.173 T at ±16 mm from the centre and a local minimum of about 0.161 T at the centreline, where the field gradient is near zero while significant gradients exist on either side of the centre.

These differences in magnetic field amplitude, spatial distribution, and gradient are expected to have a direct influence on the electromagnetic response of two-YBCO-bulk configuration. A stronger magnetic field can enhance magnetic flux penetration and activate larger shielding currents, while the spatial nonuniformity and gradient of the field affect the current distribution near the angular gap. The field gradient plays a crucial role in the Lorentz force density distribution, as the force density depends on both the local current density and the magnetic field gradient. Therefore, the comparison of the three PMG configurations in figure 2 provides the necessary magnetic field basis for analysing the subsequent shielding current evolution and levitation force variation.

3.2 Levitation force characteristics under different PMG topologies

As shown in figures 3(a), 4(a), and 5(a), the two-YBCO-bulk configuration exhibits a consistent height-dependent levitation force response under the three PMG configurations. During the descending process, the levitation force increases nonlinearly with decreasing levitation height and reaches its maximum at 10 mm. In the subsequent ascending process, the force follows a distinct return path rather than retracing the descending branch, reflecting the intrinsic hysteretic response associated with irreversible flux penetration and flux pinning in the HTS bulks.

For the FCPMG, the magnetic field distribution in figure 2(a) indicates that the magnetic flux is mainly concentrated in the central working region. Correspondingly, as shown in figure 3(a), the peak



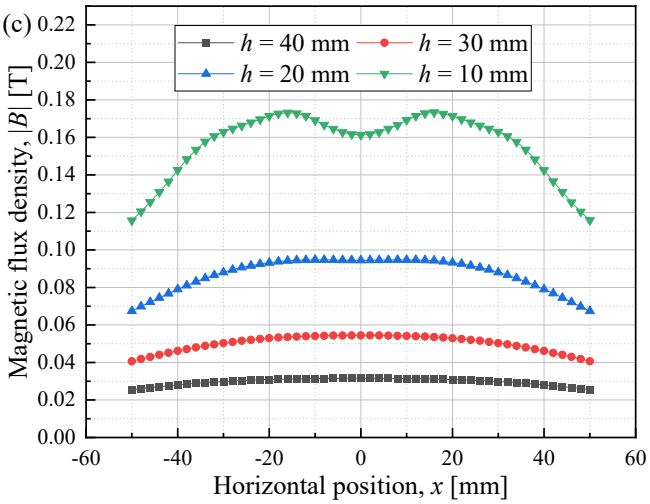


Figure 2. Magnetic flux density magnitude |B| distributions of different PMG configurations at various levitation heights. (a) Flux-concentrating PMG; (b) Surface-magnetized PMG; (c) Halbach PMG.

levitation force under the $\theta = 0°$ condition is 17.12 N. Since the angular gap is introduced near the inner boundaries of the two HTS bulks, it directly perturbs the shielding current path in a relatively high field region. As a result, the peak levitation force decreases progressively with increasing θ. The levitation force reduction rate $\eta_{pf}(\theta)$ is defined as the percentage decrease in the peak levitation force relative to the reference configuration ($\theta = 0°$), i.e.

$$\eta_{pf}(\theta) = \frac{F_{y,peak}(0^\circ) - F_{y,peak}(\theta)}{F_{y,peak}(0^\circ)} \times 100\% \tag{9}$$

As shown in figure 3(b), the reduction rates are 17.30%, 17.37%, 17.44%, 17.48%, 17.55%, 17.92%, 18.30%, 18.67%, 20.18%, 21.68%, 23.15%, and 24.58% for θ = 0.05°, 0.10°, 0.15°, 0.20°, 0.25°, 0.50°, 0.75°, 1°, 2°, 3°, 4°, and 5°, respectively. Most of the reduction relative to the continuous θ = 0° reference is already present at θ = 0.05°. Therefore, this initial change must not be interpreted as an angular sensitivity alone: it primarily reflects formation of an electrically blocking air gap. The much smaller differences among the nonzero-angle cases characterize the additional influence of gap angle. The numerical data are represented by the following empirical piecewise fit:

$$\eta_{pf}(\theta) = \begin{cases} 17.30H(\theta - 0^+), & 0 < \theta \le 0.05^\circ \\ 1.45\theta + 17.21, & 0.05^\circ \\ 1.48\theta + 17.22, & 1.0^\circ \end{cases} \tag{10}$$

where the Heaviside step function $H(x)$ is defined as follows:

$$H(x) = \begin{cases} 0, & x < 0 \\ 1, & x \ge 0 \end{cases} \tag{11}$$

The pronounced initial reduction occurs when the joined θ = 0° configuration is replaced by two separated domains at θ > 0°. It therefore reflects loss of electromagnetic continuity across the original interface, rather than a singular physical effect associated specifically with θ = 0.05° or θ = 0.25°. Once the air gap exists, increasing θ modifies the local field exposure and the already reconstructed current paths, producing a comparatively gradual additional change.

For the SMPMG, the θ = 0° peak levitation force is 10.65 N. The corresponding reduction rates are 8.61%, 8.76%, 8.86%, 8.99%, 9.11%, 9.75%, 10.37%, 10.95%, 13.32%, 15.61%, 17.80%, and 19.93% for θ = 0.05°, 0.10°, 0.15°, 0.20°, 0.25°, 0.50°, 0.75°, 1°, 2°, 3°, 4°, and 5°, respectively. As for the FCPMG, the large difference between θ = 0° and θ = 0.05° is dominated by interface separation, followed by a more gradual dependence on angle. The numerical data are represented by the following empirical piecewise fit:

$$\eta_{pf}(\theta)=\begin{cases}8.61H\left(\theta-0^{+}\right), & 0<\theta\le 0.05^{\circ}\\ 2.47\theta+8.50, & 0.05^{\circ}\ \ \ \ \\ 2.20\theta+8.86, & 1.0^{\circ}\ \ \ \ \end{cases} \tag{12}$$

The initial reduction at θ = 0.05° is 17.30% for the FCPMG and 8.61% for the SMPMG. This difference shows that loss of continuity at the central interface has a stronger electromagnetic consequence when that interface coincides with the concentrated central field of the FCPMG.

Among the separated configurations, the fitted slope for the SMPMG is larger than that for the FCPMG over both 0.05° < θ ≤ 1° (2.47%/° versus 1.45%/°) and 1° < θ ≤ 5° (2.20%/° versus 1.48%/°). Thus, after the finite gap has formed, the FCPMG response is closer to saturation, whereas the SMPMG shows a more sustained angular dependence. The FCPMG nevertheless retains the larger total reduction throughout the investigated range because of its much larger separation-induced initial change. This behavior is consistent with the different local field distributions at the gap: strong central excitation in the FCPMG activates the newly exposed boundaries immediately, whereas the smoother SMPMG field produces a smaller initial response but a larger subsequent slope.

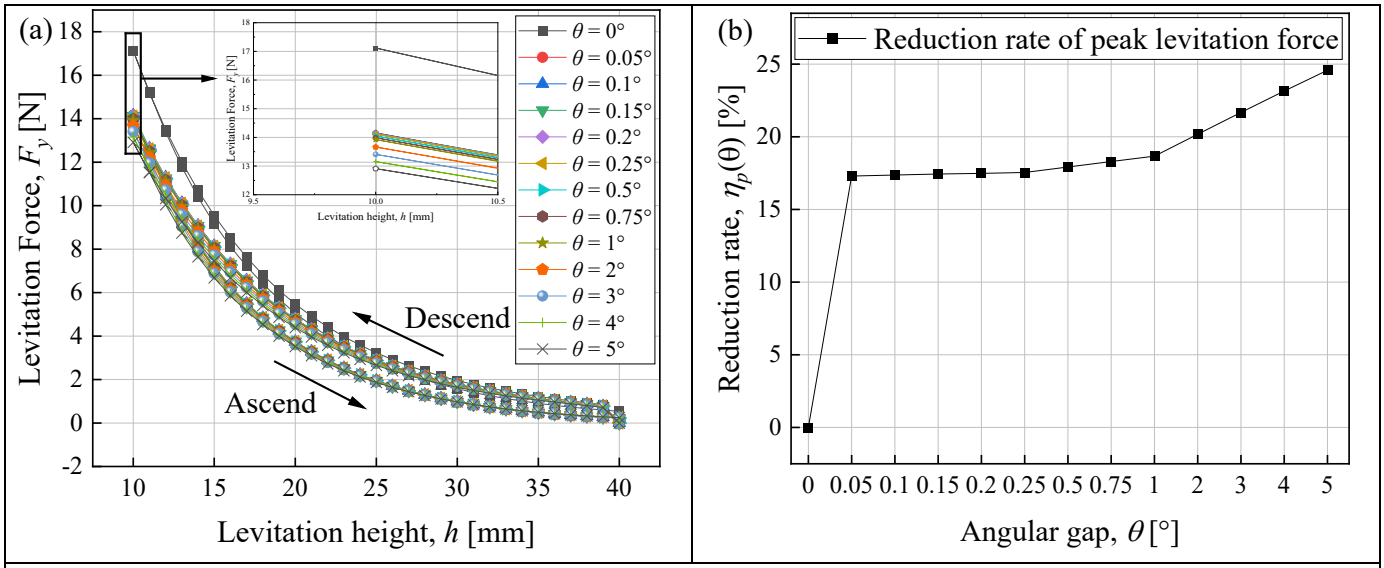


Figure 3. Effect of angular gap on the levitation force above the flux-concentrating PMG. (a) Levitation force–height curves; (b) reduction rate of peak levitation force.

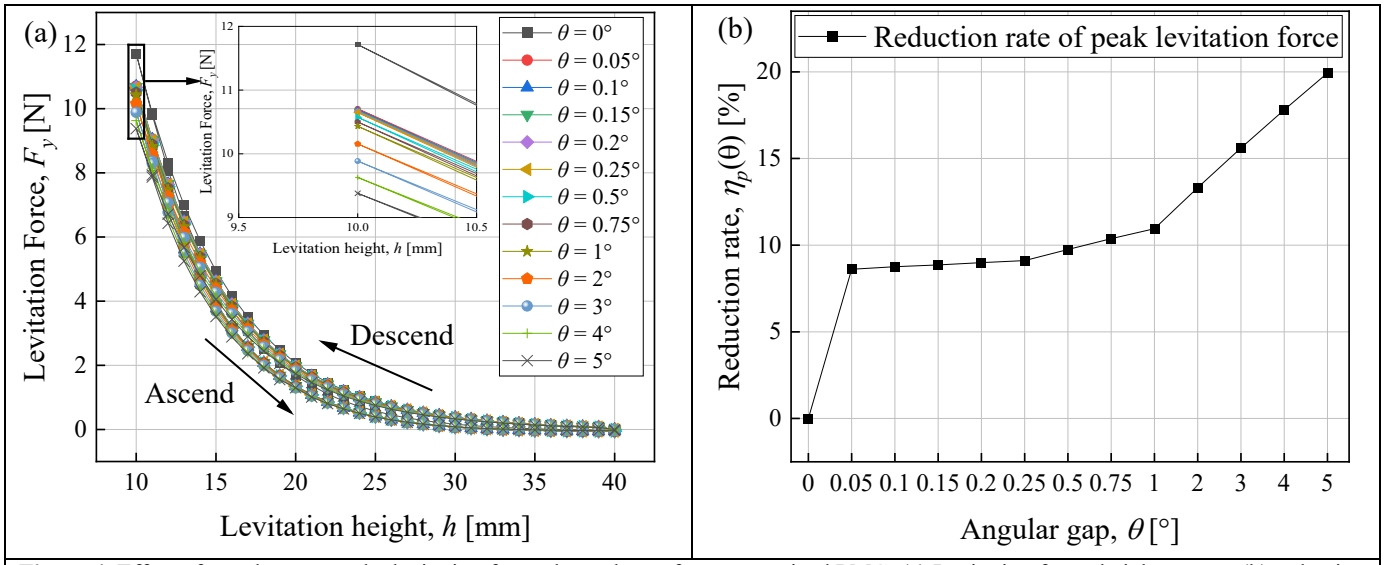


Figure 4. Effect of angular gap on the levitation force above the surface-magnetized PMG. (a) Levitation force–height curves; (b) reduction rate of peak levitation force.

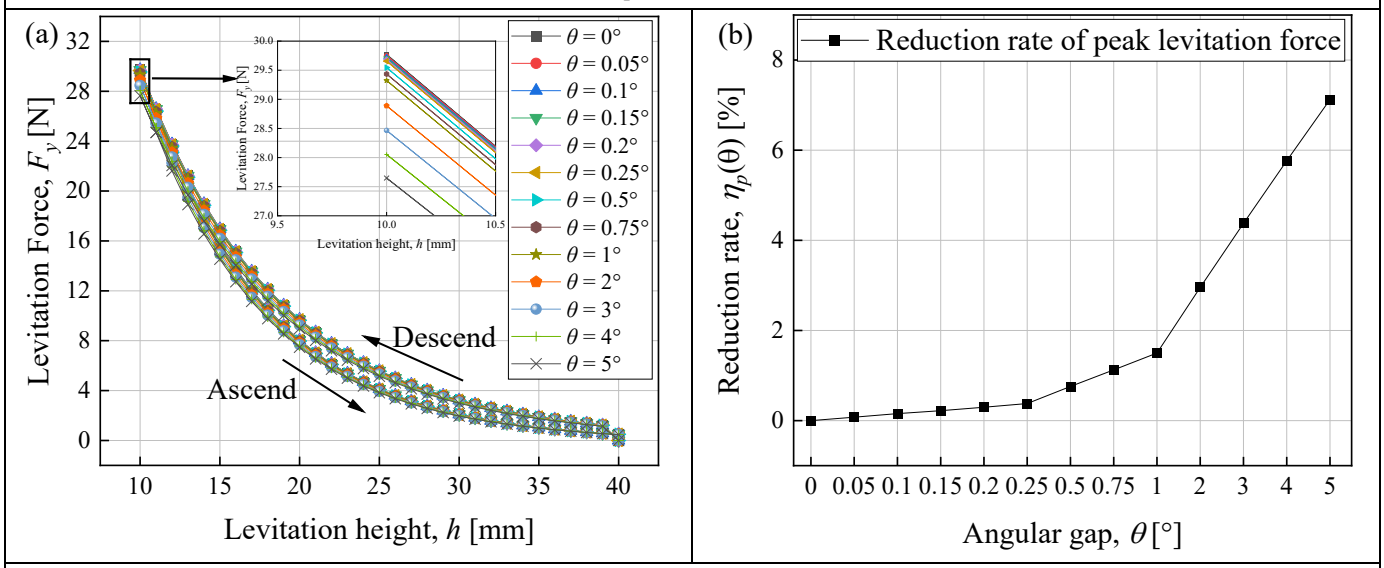


Figure 5. Effect of angular gap on the levitation force above the Halbach PMG. (a) Levitation force–height curves; (b) reduction rate of peak levitation force.

These results separate two contributions that were conflated when only θ = 0° and θ ≥ 0.25° were considered: (i) a topology-dependent change caused by formation of an electrically blocking interface and (ii) the additional dependence on opening angle among the already separated configurations.

For the HPMG, the θ = 0° peak levitation force is 29.77 N. The reduction rates are 0.07%, 0.15%, 0.22%, 0.30%, 0.38%, 0.76%, 1.13%, 1.49%, 2.96%, 4.38%, 5.77%, and 7.12% for θ = 0.05°, 0.10°, 0.15°, 0.20°, 0.25°, 0.50°, 0.75°, 1°, 2°, 3°, 4°, and 5°, respectively. Unlike the FCPMG and SMPMG, the HPMG shows no pronounced discontinuous change when the air gap first forms. Its fitted slopes are 1.50%/° for 0.05° < θ ≤ 1° and 1.41%/° for 1° < θ ≤ 5°. The numerical data are represented by the following empirical piecewise fit:

$$\eta_{pf}(\theta) = \begin{cases} 1.50\theta & 0 < \theta \le 1.0^{\circ} \\ 1.41\theta + 0.12, & 1.0^{\circ} \; \ldots \end{cases} \tag{13}$$

Equations (10), (12), and (13) are empirical curve fits to the numerical data. They are used only to summarize trends within the simulated angular range and are not theoretically derived constitutive or scaling relations.

The absence of a pronounced separation-induced drop for the HPMG is consistent with its double-peak field profile, which places the central interface in a relative field valley. The reduction increases only from 0.07% at θ = 0.05° to 0.38% at θ = 0.25°.

Table 1 summarizes the empirical fit parameters. The key distinction is whether formation of the finite gap produces a pronounced initial change relative to the continuous θ = 0° reference.

Table 1. Piecewise function parameters of the levitation force reduction rate $\eta_{pf}(\theta)$ for the three PMG configurations.

Parameter	FCPMG	SMPMG	HPMG
Pronounced initial response	Yes	Yes	No
Initial reduction at θ = 0.05°, η_0 (%)	17.3	8.6	-
First segment slope k_1 (%/°)	1.45	2.47	1.50
Second segment slope k_2 (%/°)	1.48	2.20	1.41
Boundary between segments	$\theta = 1°$	$\theta = 1°$	$\theta = 1°$
η_{pf}(5°) (%)	24.58	19.93	7.12

For the HPMG, no pronounced separation-induced initial drop is observed. The reported slopes describe the angular variation among the nonzero-gap cases.

The FCPMG and SMPMG exhibit initial reductions of 17.30% and 8.61%, respectively, at θ = 0.05°, whereas the HPMG does not show a comparable initial drop. For the already separated configurations, the fitted slopes are 1.45%/° and 1.48%/° for the FCPMG, 2.47%/° and 2.20%/° for the SMPMG, and 1.50%/° and 1.41%/° for the HPMG below and above θ = 1°, respectively. The data therefore indicate that PMG topology controls both the discontinuity-formation response and the subsequent angular dependence.

The following sections examine the corresponding shielding-current, magnetic-field, and Lorentz-force-density redistributions. Repetitive descriptions of the same force-reduction trends are avoided.

3.3 Gap induced shielding current reconstruction under different PMG configurations

During gap formation, the outer bottom corners of the bulks remain at a levitation height of 10 mm, whereas their inner bottom corners are lifted as θ increases. At θ = 0°, the interface is internal and electromagnetically continuous. For θ > 0°, it becomes two exposed superconducting–air boundaries. In a local coordinate system along an exposed inner surface, the tangential magnetic-field component is Ht = H·t, where t is the surface tangent. Spatial variation of Ht along and across the boundary is associated through Ampère's law with the out-of-plane shielding current Jz. The strong initial response therefore arises when a previously internal interface first becomes field-exposed and supports a new boundary-current path. Further increases in θ mainly modify the magnitude and distribution of this existing path. The response differs among the PMGs because Ht and its local spatial gradients at the gap depend on guideway field topology.

Owing to the geometric symmetry of the system, all statistical analyses of the shielding current density, magnetic field distribution, and Lorentz body force density within the HTS bulks are performed on a single bulk.

Figures 6, 7, and 8 respectively present the shielding current density distributions of the two-YBCO-bulk configuration at the minimum levitation height of 10 mm, which is the position where the peak levitation force is obtained. In the two-dimensional H-formulation, the induced shielding current flows along the out-of-plane direction and is given by

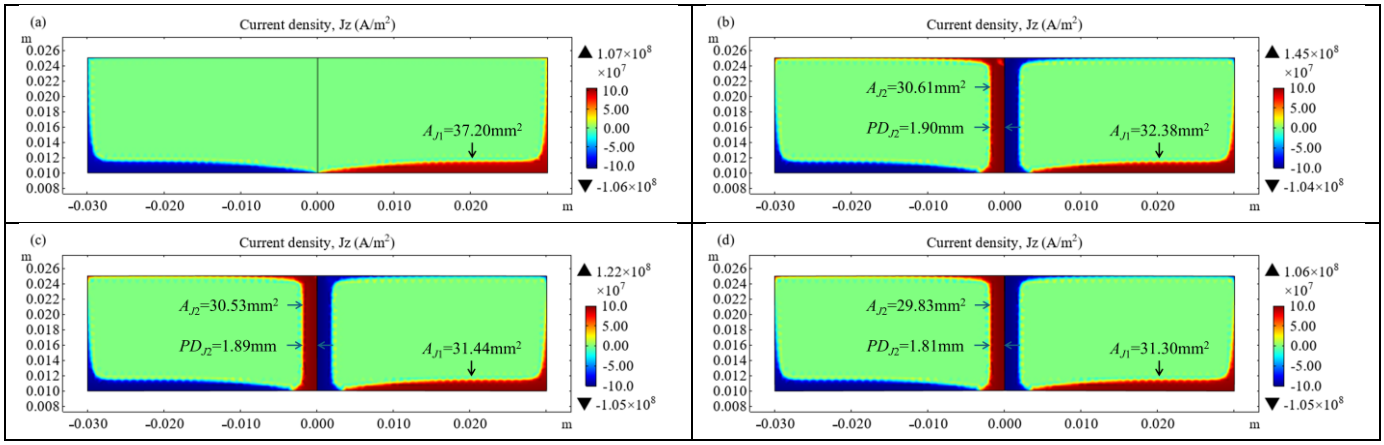
$$J_z = \frac{\partial H_y}{\partial x} - \frac{\partial H_x}{\partial y} \tag{14}$$

The J_z maps clearly reveal both the flux penetration fronts and the gap-induced redistribution of shielding current paths.

For the aligned configuration $\theta = 0°$, as shown in figures 6(a), 7(a), and 8(a), the shielding currents are largely confined to the lower edges of the HTS bulks for both the flux-concentrating and surface-magnetized PMGs, with penetration areas A_{J1} of 37.20 mm² and 28.37 mm², respectively. For the Halbach PMG, the shielding currents are mainly distributed along both the lower and outer edges, with penetration areas of $A_{J1} = 33.85$ mm^2 and $A_{J3} = 40.47$ mm^2, respectively.

At θ = 0.05°, the newly exposed inner boundaries of the FCPMG and SMPMG cases become additional flux-penetration fronts and support opposite-polarity current layers. The induced inner-boundary current areas are 30.61 mm² and 18.29 mm², with penetration depths of 1.90 mm and 1.00 mm, respectively. No comparable inner-edge layer appears for the HPMG, although its pre-existing lower- and outer-edge currents are modified. In table 2, the HPMG areas AJ1 and AJ3 decrease by 0.7% and 5.4%, respectively, at θ = 0.05°, and by 10.7% and 20.0% at θ = 5°.

For the FCPMG and SMPMG, the inner-boundary current areas decrease from 30.61 and 18.29 mm² at θ = 0.05° to 26.57 and 16.45 mm² at θ = 1°, respectively. At θ = 5°, they decrease further to 23.90 and 15.72 mm². The penetration patterns also become increasingly asymmetric along the inclined inner boundaries. These observations show that formation of the gap creates a new current topology, whereas subsequent increases in θ progressively modify its area, depth, and spatial distribution.



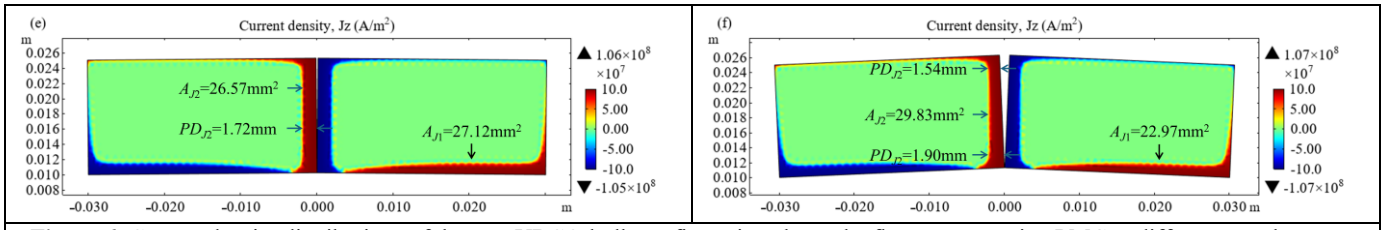


Figure 6. Current density distributions of the two-YBCO-bulk configuration above the flux-concentrating PMG at different angular gaps. (a) $\theta = 0°$; (b) $\theta = 0.05°$; (c) $\theta = 0.15°$; (d) $\theta = 0.25°$; (e) $\theta = 1°$; (f) $\theta = 5°$.

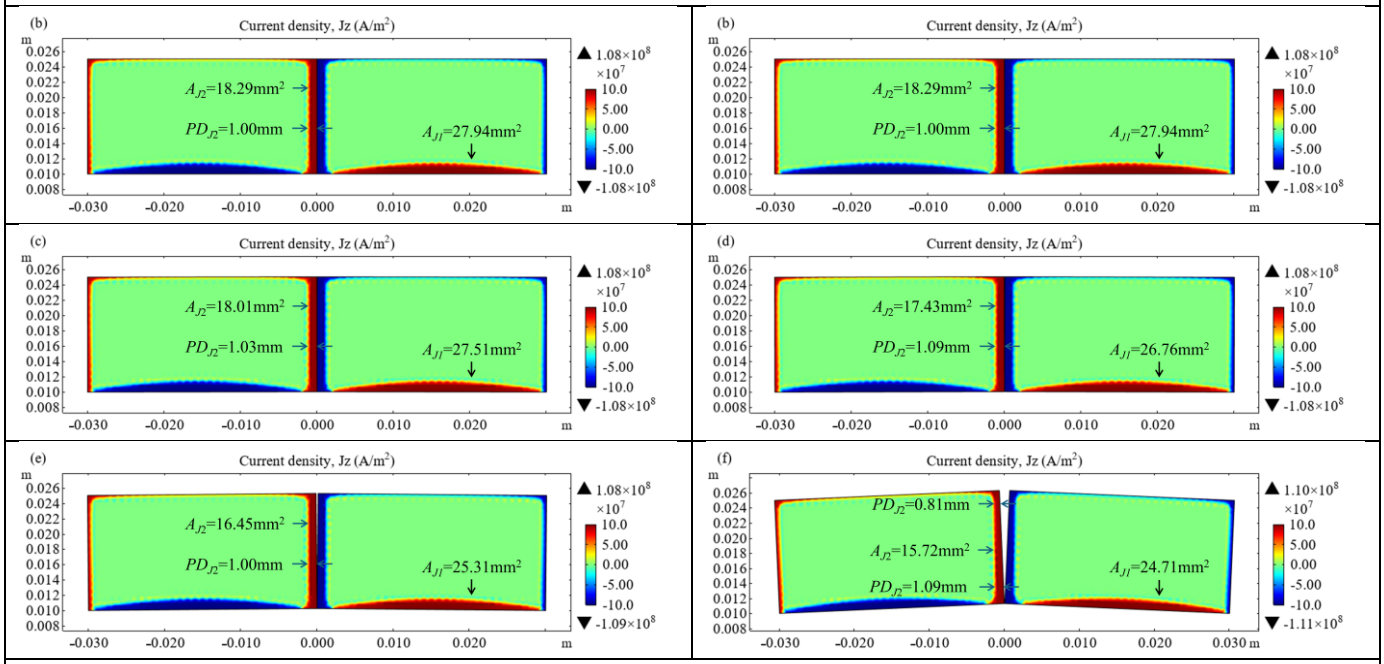


Figure 7. Current density distributions of the two-YBCO-bulk configuration above the surface-magnetized PMG at different angular gaps. (a) $\theta = 0°$; (b) $\theta = 0.05°$; (c) $\theta = 0.15°$; (d) $\theta = 0.25°$; (e) $\theta = 1°$; (f) $\theta = 5°$.

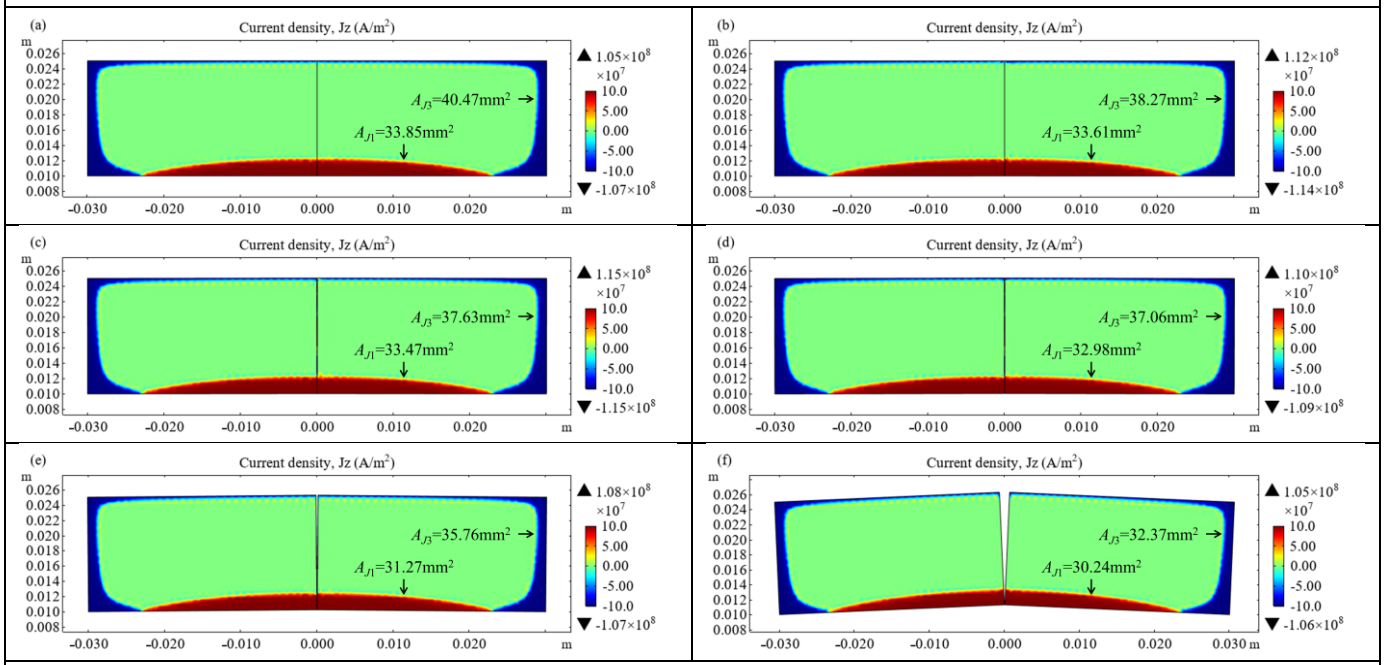


Figure 8. Current density distributions of the two-YBCO-bulk configuration above the Halbach PMG at different angular gaps. (a) $\theta = 0°$; (b) $\theta = 0.05°$; (c) $\theta = 0.15°$; (d) $\theta = 0.25°$; (e) $\theta = 1°$; (f) $\theta = 5°$.

emergence of new shielding currents at the inner edges of the superconducting bulks. The new shielding currents are strongly correlated with the PMG configuration. As the angular gap increases, both the penetration area and penetration depth of the shielding currents decrease.

Table 2 summarizes the current-penetration areas for θ = 0°, 0.05°, 0.15°, 0.25°, 1°, and 5°. The area-reduction rates are defined relative to the continuous θ = 0° reference.

$$\eta_{AB}(\theta) = \frac{A_{J1}(0) - A_{J1}(\theta)}{A_{J1}(0)} \times 100\% \tag{15}$$

$$\eta_{AO}(\theta) = \frac{A_{J3}(0) - A_{J3}(\theta)}{A_{J3}(0)} \times 100\% \tag{16}$$

Figures 6, 7, and 8 show that the gap-boundary current response is governed by the spatial correspondence between the local magnetic field and the gap position rather than by the overall field strength. The central field concentration of the FCPMG produces the strongest gap-boundary current activation, while the smoother SMPMG field produces a moderate response. In contrast, the central gap of the HPMG lies in a relative field valley, resulting in the weakest inner-boundary response despite its higher overall magnetic flux density. Once the finite gap is formed, subsequent increases in θ mainly modify the penetration area and depth of the reconstructed current pattern. These results confirm that the angular-gap effect is essentially a local field–geometry matching process.

3.4 Internal magnetic flux density redistribution under different PMG configurations

In the two-dimensional model, the shielding current flows along the out-of-plane direction. The vertical Lorentz body force density f_y is determined by the coupling between J_z and the internal horizontal magnetic flux density component B_x, i.e. $f_y = J_z B_x$. Therefore, before examining f_y, this

Table 2. Variation of shielding current areas with angular gap for different PMG configurations.

Angular gap/°	FCPMG		SMPMG		HPMG			
	A_{J1}/ mm^2	η_{AB} /%	A_{J1}/ mm^2	η_{AB} /%	A_{J1}/ mm^2	η_{AB} /%	A_{J3}/ mm^2	η_{AO} /%
0°	37.20	/	28.37	/	33.85	/	40.47	/
0.05	32.28	13.2	27.94	1.5	33.61	0.7	38.27	5.4
0.15	31.44	15.5	27.51	3.0	33.47	1.1	37.63	7.0
0.25°	31.30	15.9	26.76	5.7	32.98	2.6	37.06	8.4
1°	27.12	27.1	25.31	10.8	31.27	7.6	35.76	11.6
5°	22.97	38.2	24.71	12.9	30.24	10.7	32.37	20.0

The vertical Lorentz body-force density fy is governed by the product of the out-of-plane current density and the horizontal magnetic-flux-density component, fy = JzBx. Figures 9–11 therefore show Bx for θ = 0°, 0.05°, 0.15°, 0.25°, 1°, and 5°.

For the FCPMG, the lower-region Bx distribution is displaced outward as the gap forms and opens. The distance dB1 increases from 1.09 mm at θ = 0° to 3.49, 3.56, 3.62, 3.80, and 4.43 mm at θ = 0.05°, 0.15°, 0.25°, 1°, and 5°, respectively. The corresponding lower-region areas decrease from 33.41 mm² to 32.14, 31.54, 30.15, 29.70, and 25.96 mm². At θ = 0.05°, additional localized Bx regions appear near the upper and lower inner corners, with areas of 4.97 and 3.14 mm², respectively. The maximum Bx decreases from 0.176 T at θ = 0° to 0.166 T at θ = 0.05° and remains nearly unchanged at the larger angles considered.

For the SMPMG configuration, as shown in figures 10(a)–10(f), the introduction of the angular gap induces internal magnetic fields at the inner corners of the superconducting bulk, including both the upper and lower inner corners, similar to the FCPMG case. Meanwhile, the bottom magnetic field is upper and lower inner corners, similar to the FCPMG case. Meanwhile, the bottom magnetic field is progressively displaced away from the central axis as the gap angle increases, which is also consistent with the behaviour observed in the FCPMG configuration. However, a notable difference lies in the

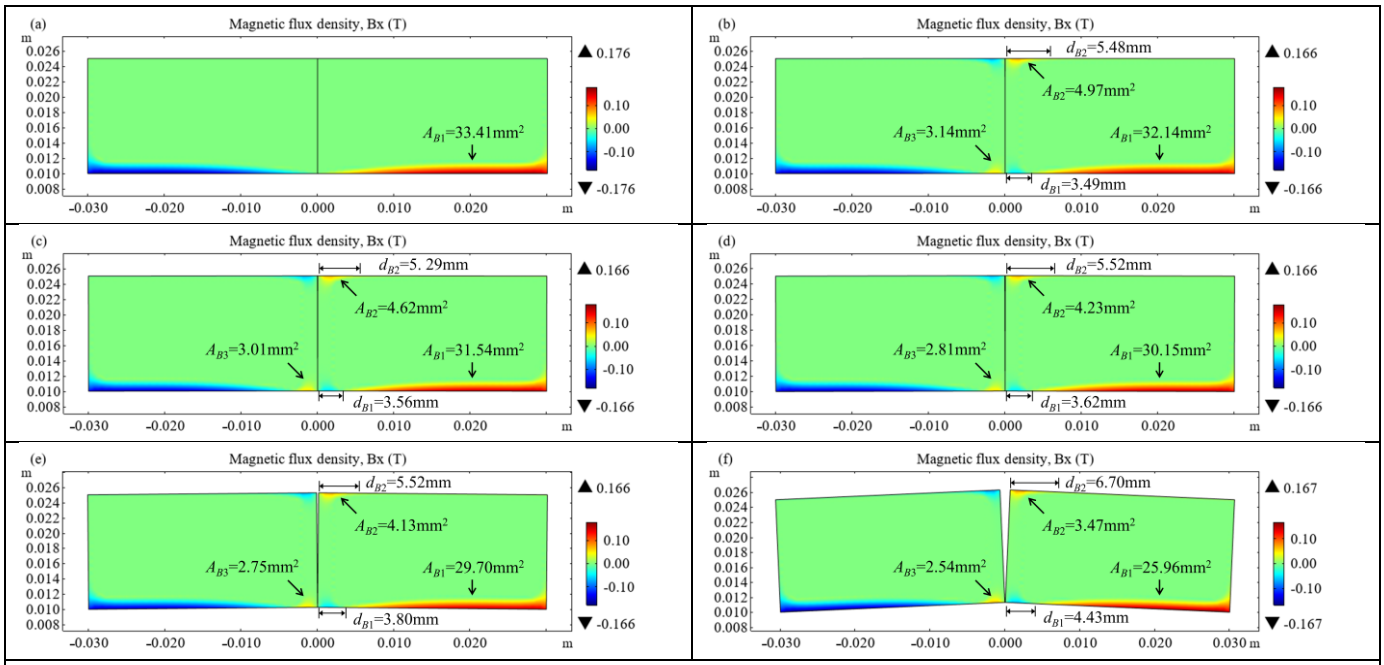
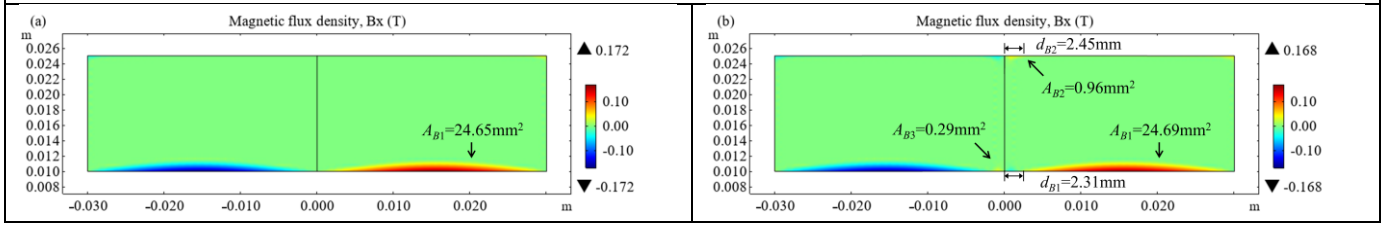


Figure 9. Internal horizontal magnetic flux density distributions of the two-YBCO-bulk configuration above the flux-concentrating PMG at different angular gaps. (a) θ = 0°; (b) θ= 0.05°; (c) θ= 0.15°; (d) θ= 0.25°; (e) θ= 1°; (f) θ= 5°.



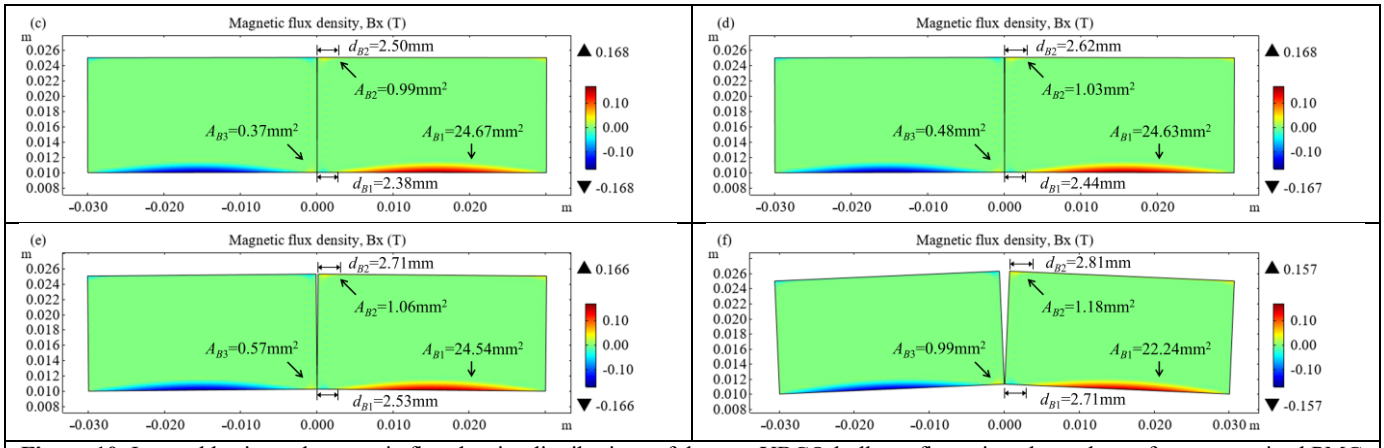


Figure 10. Internal horizontal magnetic flux density distributions of the two-YBCO-bulk configuration above the surface-magnetized PMG at different angular gaps. (a) $\theta = 0°$; (b) $\theta = 0.05°$; (c) $\theta = 0.15°$; (d) $\theta = 0.25°$; (e) $\theta = 1°$; (f) $\theta = 5°$.

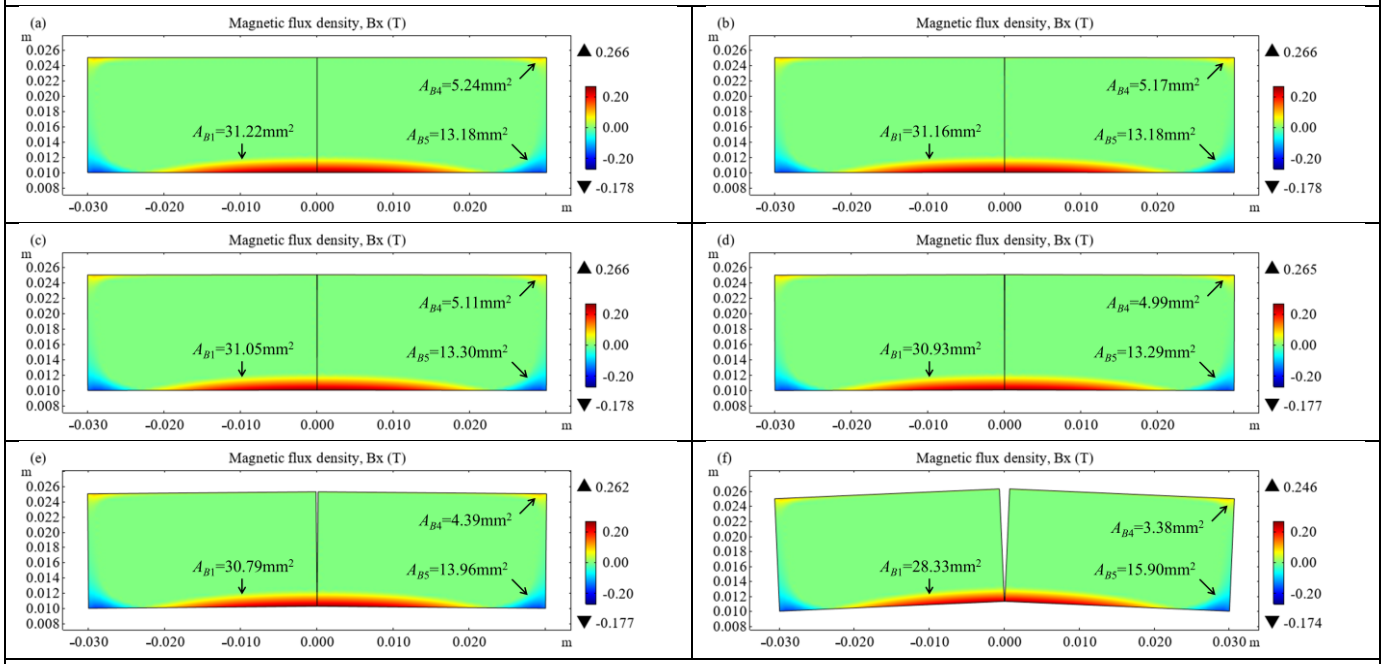


Figure 11. Internal horizontal magnetic flux density distributions of the two-YBCO-bulk configuration above the Halbach PMG at different angular gaps. (a) $\theta = 0°$; (b) $\theta = 0.05°$; (c) $\theta = 0.15°$; (d) $\theta = 0.25°$; (e) $\theta = 1°$; (f) $\theta = 5°$.

shape of the bottom magnetic field B_x distribution. For the SMPMG, the bottom B_x field exhibits a parabolic profile, which is similar to the shape of the shielding current distribution. In contrast, the FCPMG displays an approximately L-shaped distribution, which is roughly consistent with its shielding current morphology. Furthermore, owing to the spatial variation of the magnetic field near the central axis in the SMPMG, the magnetic field intensity at the inner corners tends to increase with the angular gap. Specifically, for gap angles $\theta = 0.05°$, 0.15°, 0.25°, 1°, and 5°, the B_x distribution areas at the upper inner corner, denoted as A_{B2}, are 0.96 mm², 0.99 mm², 1.03 mm², 1.06 mm², and 1.18 mm², respectively. At the lower inner corner, the corresponding areas A_{B3} increase from 0.29 mm² to 0.57 mm² and 0.99 mm². Regarding the extreme values of the magnetic field, the appearance of the angular gap in the SMPMG configuration results in a 0.004 T decrease in the B_x peak value, as illustrated in figures 10(a) and 10(b). With increasing gap angle, the maximum B_x exhibits its largest decline at 5°, with a reduction of 0.015 T, equivalent to a reduction rate of 8.7%.

As shown in figures 11(a)-(f), for the HPMG configuration, the internal magnetic field B_x distribution within the superconductor is similar to the current distribution, being located at the outer corners and the bottom of the bulk, with no additional magnetic field generated at the inner side of the bulk near the angular gap. The distribution of field magnitudes follows the same trend as the other two configurations, where the highest B_x values occur at the outer side, and the field strength gradually decreases toward the interior of the superconductor. However, the distribution region and shape differ from the previous two configurations. The bottom magnetic field exhibits a nearly uniform distribution in the central region, with a gradual decrease toward the outer sides. As the angular gap increases, the bottom field area A_{B1} gradually decreases from 31.22 mm² in the absence of the gap to 28.33 mm² at $\theta = 5°$. At the upper outer corner, the positive magnetic field area A_{B4} decreases from 5.24 mm² to 3.38 mm². Meanwhile, the negative magnetic field area A_{B5} at the lower outer corner increases from 13.18 mm² to 15.90 mm² at 5°.

3.5 Quantitative analysis of Lorentz force density region areas

Based on the J_z distributions (section 3.3) and Bx distributions (section 3.4), this section quantifies the resulting Lorentz body force density $f_y = J_z B_x$. The areas of positive and negative force regions are measured from the f_y maps to establish the quantitative link between local force redistribution and global levitation force degradation.

To facilitate quantitative analysis, the f_y maps are divided into four categories based on the sign and magnitude of the vertical Lorentz force density: the primary positive-force region (f_y >0, with large magnitude), the secondary positive-force region (f_y >0, with small magnitude), the negative-force region (f_y <0), and the weak-force region ($|f_y| < \varepsilon$), where ε is a small threshold. The areas of these regions are denoted as A_{pos}^{pri}, A_{pos}^{sec}, A_{neg}, and A_{weak}, respectively.

Under the single-peak field configuration of the FCPMG, in the absence of an angular gap, the Lorentz force density map in figure 12(a) consists only of the primary positive-force region and the weak-force region. The primary positive-force region is located at the bottom of the bulk, with its magnitude increasing from the inner to the outer side, and its area is $A_{pos}^{pri} = 30.47 mm^2$. Once the angular gap is introduced (figure 12(b), $\theta = 0.05°$), the original two regions are replaced by four distinct regions. A negative-force region and a secondary positive-force region emerge at the upper and lower portions of the inner side of the bulk, respectively. These two regions arise from the induced inner-side shielding currents and the associated internal magnetic fields at these positions. Although their areas are relatively small ($A_{neg} = 3.74 mm^2$ and $A_{pos}^{sec} = 1.75 mm^2$), the presence of the secondary positive-force region displaces the primary positive-force region outward by $D_{pos}^{pri} = 3.96 mm$. Concurrently, the peak force density of the primary positive-force region drops from 1.76×10^7 N/mm^3 to 1.65×10^7 N/mm^3. These observations indicate that the outward shift, the reduction in area, and the decrease in the peak value of

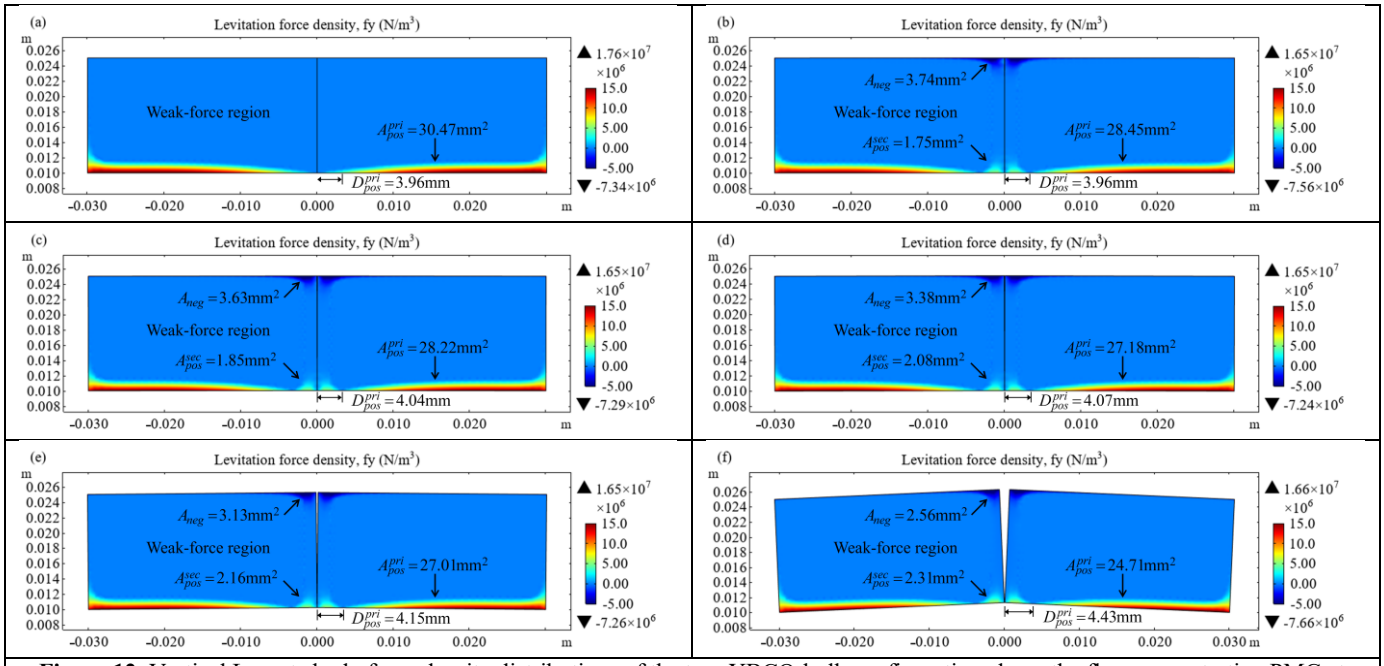


Figure 12. Vertical Lorentz body force density distributions of the two-YBCO-bulk configuration above the flux-concentrating PMG at different angular gaps. (a) θ = 0°; (b) θ= 0.05°; (c) θ= 0.15°; (d) θ= 0.25°; (e) θ= 1°; (f) θ= 5°.

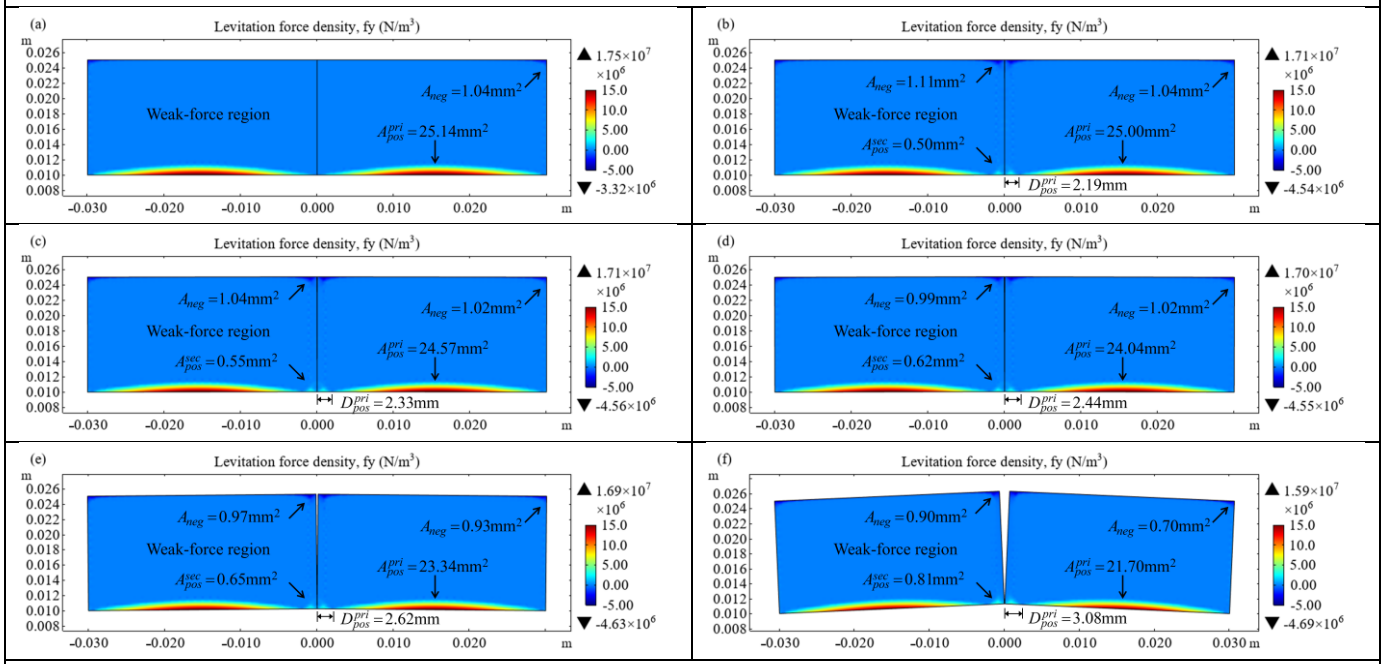
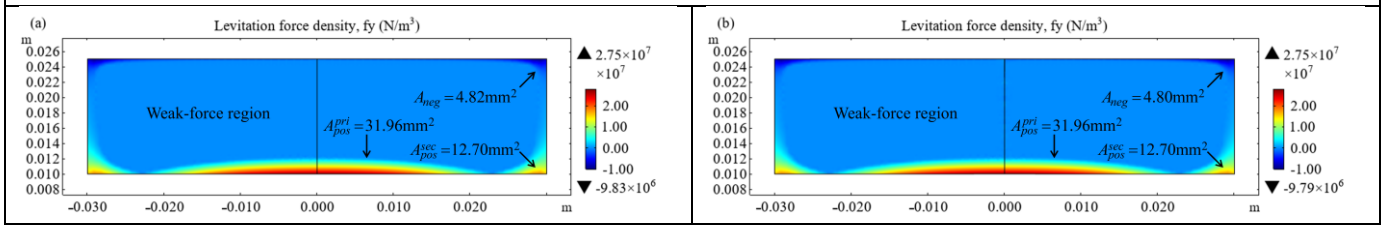


Figure 13. Vertical Lorentz body force density distributions of the two-YBCO-bulk configuration above the surface-magnetized PMG at different angular gaps. (a) θ = 0°; (b) θ= 0.05°; (c) θ= 0.15°; (d) θ= 0.25°; (e) θ= 1°; (f) θ= 5°.



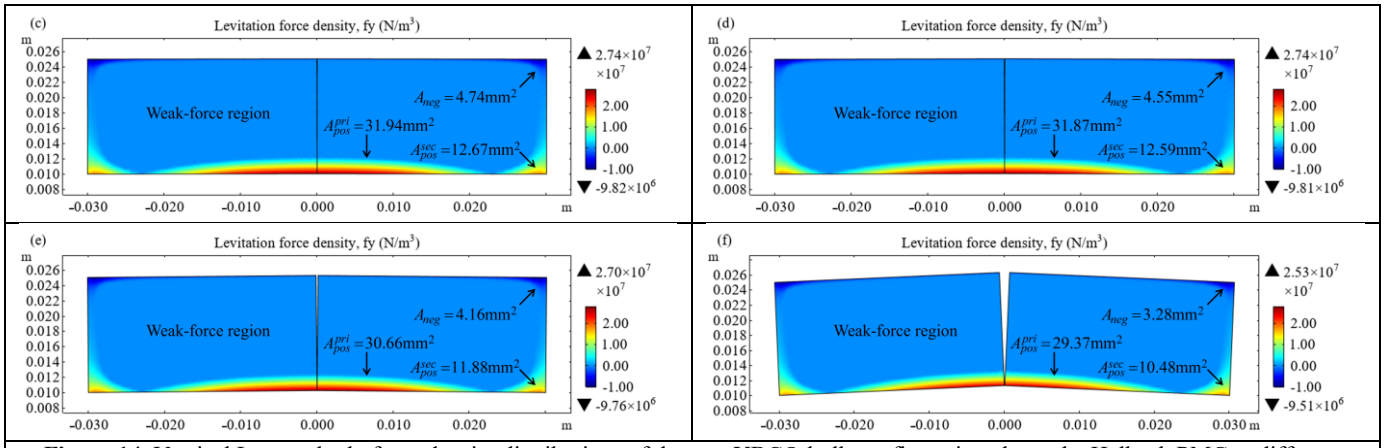


Figure 14. Vertical Lorentz body force density distributions of the two-YBCO-bulk configuration above the Halbach PMG at different angular gaps. (a) $\theta = 0°$; (b) $\theta = 0.05°$; (c) $\theta = 0.15°$; (d) $\theta = 0.25°$; (e) $\theta = 1°$; (f) $\theta = 5°$.

the primary positive-force region are the primary factors responsible for the sharp degradation of levitation force. As θ further increases to 1° and 5°, with the inner side of the bulks being progressively lifted, the negative-force region shrinks gradually, while the secondary positive-force region undergoes a slight expansion. Nevertheless, the primary positive-force region exhibits a marked reduction in area: from 27.01 mm² at $\theta = 1°$ to 24.71 mm² at $\theta = 5°$, amounting to a total decrease of 18.9%.

Under the surface-uniform field configuration of the SMPMG, in the absence of an angular gap, the primary positive-force region is situated at the bottom of the bulk, displaying a parabolic profile from the inner to the outer side, with a distribution area of $A_{pos}^{pri} = 25.14mm^2$, as shown in figure 13(a). The abscissa of the parabolic vertex approximately coincides with the peak position of the SMPMG magnetic field. Once the angular gap is introduced at $\theta = 0.05°$ (figure 13(b)), a negative-force region and a secondary positive-force region emerge at the upper and lower inner sides of the bulk, respectively. The areas of these two regions are comparatively smaller than those in the FCPMG configuration. Nevertheless, the bottom primary positive-force region still experiences a notable outward shift, peak attenuation, and area reduction. At gap angles of 0.05°, 0.15°, 0.25, 1° and 5°, the primary positive-force region shifts outward by 2.19 mm, 2.33 mm,2.44 mm, 2.62 mm, and 3.08 mm, respectively. Concurrently, the peak positive force density decreases from 1.75×10^7 N/mm^3 to 1.59×10^7 N/mm^3 at 5°, yielding a peak reduction rate of 9.1%. The area of the primary positive-force region decreases to 25.00 mm², 24.57 mm², 24.04 mm², 23.34 mm², and 21.70 mm², corresponding to reduction rates of 0.6%, 2.2%, 4.5%, 7.2%, and 13.8%, respectively.

In contrast to the force influences observed in the preceding two magnetic field configurations, the Lorentz force density distribution within the superconducting bulk under the HPMG double-peak field configuration consistently comprises four regions, namely the primary positive-force region, the secondary positive-force region, the weak-force region, and the negative-force region, regardless of the angular gap magnitude, as shown in figures 14(a)–14(f) for $\theta = 0°$, 0.05°, 0.15°, 0.25°, 1°, and 5°. The primary positive-force region is situated at the bottom of the bulk, with its magnitude decreasing from the inner side to the outer side. The secondary positive-force region and the negative-force region are located at the lower outer corner and the upper outer corner of the bulk, respectively. As θ increases

from 0° to 0.05°, 0.15°, 0.25°, 1°, and 5°, the area of the primary positive-force region decreases from 31.96 mm² to 31.96 mm², 31.94 mm², 31.87 mm², 30.66 mm², and 29.37 mm², yielding a final reduction rate of 8.1%. The area of the secondary positive-force region constitutes approximately 35.7%–39.7% of the primary positive-force region area. The negative-force region area decreases from 4.82 mm² to 3.28 mm². The peak force density consistently resides in the primary positive-force region, decreasing from 2.75×10^7 N/mm^3 at $\theta = 0°$ to 2.53×10^7 N/mm^3 at $\theta = 5°$. The peak value of the secondary positive-force region ranges between 58% and 67% of that of the primary region. These observations indicate that the reduction in force density within the bottom primary positive-force region is the primary contributor to the levitation force degradation under the HPMG configuration.

As the angular gap increases to $\theta = 1°$ and 5°, the negative body force region near the gap boundary persists, while the bottom side positive force density band is further modified by the relative rotation of the two HTS bulks. This indicates that the angular gap changes not only the shielding current topology, but also the balance between positive and negative Lorentz body force contributions. In other words, part of the electromagnetic response is transferred from the bottom side force generating region to the inner gap boundary, where the resulting force contribution is weak or even negative. Consequently, the integrated levitation force decreases even though strong local shielding currents may still exist near the gap.

The three PMG configurations exhibit different degrees of force density redistribution. For the FCPMG, the central magnetic excitation promotes the strongest gap boundary current reconstruction, and the negative body force density near the gap is correspondingly the most evident. For the SMPMG, the smoother field distribution leads to a more moderate gap boundary response and a weaker negative force density region. For the HPMG, the strongest B_x and positive body force density remain concentrated near the bottom side of the bulks, which explains its higher overall levitation force level. Nevertheless, a local negative body force density still appears near the angular gap, indicating that the gap introduces an unfavorable local force contribution even when the global magnetic excitation is strong.

Overall, the combined B_x and f_y analyses reveal that the reduction in peak levitation force is governed by the redistribution of effective Lorentz body force density. The angular gap redirects part of the shielding current toward the inner boundary, but this region does not coincide with the main favorable B_x distribution. As a result, the positive force contribution near the lower edge is weakened, while a local negative force contribution is generated near the gap boundary. The relative proportion of negative body force density therefore provides a direct physical indicator of the peak levitation force reduction rate under different angular gaps and guideway magnetic topologies.

However, the B_x distribution alone cannot explain the abrupt reduction in peak levitation force after a very small angular gap is introduced. The key lies in the spatial coupling between B_x and the gap induced shielding current redistribution shown in figures 6, 7 and 8. When $\theta = 0°$, the shielding currents and the dominant B_x component are both mainly distributed near the lower side of the bulks, leading to a concentrated positive body force contribution along the bottom edge, as shown in figures 12(a), 13(a), and 14(a). In this state, the central interface contributes little to the vertical force. Once a finite angular gap is formed, even at $\theta = 0.05°$, the inner boundaries become active current reconstruction regions.

Although the local Bx component near the gap is not visually strong in figures 9, 10 and 11, the concentrated gap boundary *Jz* can still couple with the local B_x component with an unfavorable sign, producing a distinct negative body force density near the upper part of the gap boundary, as shown in figures 12(b), 13(b), and 14(b). At the same time, the dominant positive force density band near the lower edge is weakened or redistributed. Therefore, the sharp initial reduction in peak levitation force is not a simple geometrical effect caused by the small inclination angle, but an electromagnetic consequence of current path reconstruction and the emergence of local negative force contribution.

4. Conclusions

This study numerically investigated the influence of angular gaps on the electromagnetic response and levitation performance of two-YBCO-bulk configurations above three representative PMG configurations. The main conclusions are as follows.

1. PMG field topology strongly affects the response to formation and enlargement of an angular gap. At $\theta = 5°$, the peak-force reduction is 24.58% for the FCPMG, 19.93% for the SMPMG, and 7.12% for the HPMG. These differences are associated with the spatial relation between the central interface and the local guideway field.

2. The comparison between the continuous $\theta = 0°$ reference and the separated $\theta > 0°$ configurations must be interpreted as an interface-formation effect. At $\theta = 0.05°$, the FCPMG and SMPMG already show reductions of 17.30% and 8.61%, whereas the HPMG changes by only 0.07%. Among the nonzero-angle cases, further opening produces a gradual additional change. Shielding-current and Lorentz-force-density maps show that the newly exposed inner boundaries reconstruct the current paths, introduce an unfavorable local force contribution, and weaken the main positive-force region.

3. Among the three configurations and within the dimensions, centered lateral position, levitation-height range, motion path, material law, and angular range investigated here, the HPMG gives the least degradation. This result should not be generalized to all systems containing gaps or defects. Gap sensitivity may change with lateral offset, bulk-to-PMG size ratio, levitation height, three-dimensional geometry, or interfacial material properties. Microscopic cracks and inclusions require dedicated models and cannot be predicted quantitatively from the present macroscopic air-gap results.

References

[1] Ma K B, Postrekhin Y V and Chu W K 2003 *Rev. Sci. Instrum.* **74** 4989

[2] Durrell J H, Ainslie M D, Zhou D, Vanderbemden P, Bradshaw T, Speller S C, Filipenko M and Cardwell D A 2018 *Supercond. Sci. Technol.* **31** 103501

[3] Ozturk K, Abdioglu M and Karaahmet Z 2020 *Physica C* **578** 1353739

[4] Zhang B Q, Zhang Q Q, He P, Ma Y B, Shen L, Zhang X Y and Zhou Y H 2021 *Adv. Funct. Mater.* **31** 2100680

[5] Zhou X C, Luo Y, He Y C, Peng C, Zeng P Y, Li Y and Deng Z G 2024 *Cryogenics* **141** 103892

[6] Fang X Y, Wang X L, Fang J and Li W L 2024 *Supercond. Sci. Technol.* **37** 125009

[7] Wang J S, Wang S Y, Zeng Y W, Huang H Y, Luo F, Xu Z P, Tang Q X, Lin G B, Zhang C F, Ren Z Y, Zhao G M, Zhu D G, Wang S H, Jiang H, Zhu M, Deng C Y, Hu P F, Li C Y, Liu F, Lian J S, Wang X R, Wang L H, Shen X M and Dong X G 2002 *Physica C* **378–381** 809

[8] Deng Z G, Zhang W H, Zheng J, Ren Y, Jiang D H, Zheng X X, Zhang J H, Gao P F, Lin Q X, Song B and Deng C Y 2016 *IEEE Trans. Appl. Supercond.* **26** 3602408
[9] Li H M, Shi J L, Li X D, Zhang J B and Chen Y L 2023 *Railw. Sci.* **2** 327
[10] Wang X F, Hu X, Wang J K, Wang L, Li H T, Deng Z G and Zhang W H 2023 *Proc. Inst. Mech. Eng. C J. Mech. Eng. Sci.* **237** 2279
[11] Deng Z G, Zhang W F, Chen Y, Yang X, Xia C C and Zheng J 2020 *Supercond. Sci. Technol.* **33** 034009
[12] Chen Y, Zhang X, Zheng J and D'Ovidio G 2021 *IEEE Trans. Appl. Supercond.* **31** 3603104
[13] Zhang X, Zheng J, Liu J X, Li J, Zhang W H, Cheng N, Hu Z X and Deng Z G 2022 *J. Alloys Compd.* **902** 163809
[14] Feng Y C, Zheng J, Deng Z G, Lei W Y and Wang Z L 2022 *J. Alloys Compd.* **929** 167342
[15] Namburi D K, Shi Y H and Cardwell D A 2021 *Supercond. Sci. Technol.* **34** 053002
[16] Shi Y H, Mousavi T, Dennis A R, Ainslie M D, Speller S C, Grovenor C R H, Durrell J H and Cardwell D A 2022 *Supercond. Sci. Technol.* **35** 105002
[17] Naito T, Fujishiro H and Awaji S 2019 *J. Appl. Phys.* **126** 243901
[18] Zhang Y F, Zhang Y, Shen S Y, Ruan G J, Zhang J Y, Zhang P H and Xu Y 2024 *J. Phys.: Conf. Ser.* **2671** 012011
[19] Zmorayová K, Diko P, Volochová D, Antal V, Hlásek T, Plecháček V and Antončík F 2023 *Ceram. Int.* **49** 22177
[20] Houbart M, Fagnard J F, Dular J, Dennis A R, Namburi D K, Durrell J H, Geuzaine C, Vanderheyden B and Vanderbemden P 2022 *Supercond. Sci. Technol.* **35** 064005
[21] Tutt N, Congreve J, Shi Y H, Namburi D K, Dennis A R, Druiff H and Durrell J H 2023 *Supercond. Sci. Technol.* **36** 085004
[22] Xue F, Wang J, Long J and Gou X F 2026 *Acta Mech. Sin.* **42** 425627
[23] Li H, Huang L L and Huang Y 2023 *AIP Adv.* **13** 105232
[24] An D M, Shi P P and Gou X F 2024 *Eng. Fract. Mech.* **295** 109794
[25] Shen H T, Yong H D and Zhou Y H 2024 *Eur. J. Mech. A Solids* **103** 105138
[26] Xia J and Zhou Y H 2015 *Cryogenics* **69** 1
[27] Shen B, Grilli F and Coombs T A 2020 *Supercond. Sci. Technol.* **33** 033002
[28] Ainslie M D, Grilli F, Quéval L, Pardo E, Perez-Mendez F, Mataira R, Morandi A, Ghabeli A, Bumby C W and Brambilla R 2020 *Supercond. Sci. Technol.* **33** 105009
[29] Berrospe-Juarez E, Trillaud F, Zermeño V M R and Grilli F 2021 *Supercond. Sci. Technol.* **34** 044002
[30] Arsenault A, de Sousa Alves B and Sirois F 2021 *IEEE Trans. Appl. Supercond.* **31** 6900109
[31] Huber F, Song W J, Zhang M and Grilli F 2022 *Supercond. Sci. Technol.* **35** 043003
[32] Riva N, Halbach A, Lyly M, Messe C, Ruuskanen J and Lahtinen V 2023 *IEEE Trans. Appl. Supercond.* **33** 4900405
[33] Grilli F, Morandi A, De Silvestri F and Brambilla R 2018 *Supercond. Sci. Technol.* **31** 125003
[34] Sass F, Sotelo G G, de Andrade Junior R and Sirois F 2015 *Supercond. Sci. Technol.* **28** 125012
[35] Eley S, Glatz A and Willa R 2022 *Appl. Phys. Lett.* **121** 230501
[36] Kim Y B, Hempstead C F and Strnad A R 1963 *Phys. Rev.* **129** 528
[37] Liu Y, Ding X P and Zhao X F 2026 *Phys. Scr.* **101** 185911
[38] Halbach K 1980 *Nucl. Instrum. Methods* **169** 1

[39] Zhou D J, Zhu L M, Liu J, Cai F N, Xu T, Wang L L, Chen Y H, Cheng C H and Zhao Y 2022 *IEEE Trans. Appl. Supercond.* **32** 3602908